A prototype table-top inverse-geometry volumetric CT system

Taly Gilat Schmidt[a)]
Department of Radiology, Stanford University, Stanford, California 94305

Josh Star-Lack
NexRay, Inc., Los Gatos, California 95032

N. Robert Bennett and Samuel R. Mazin[b)]
Department of Radiology, Stanford University, Stanford, California 94305

Edward G. Solomon
NexRay, Inc., Los Gatos, California 95032

Rebecca Fahrig and Norbert J. Pelc[b)]
Department of Radiology, Stanford University, Stanford, California 94305

(Received 18 August 2005; revised 10 March 2006; accepted for publication 15 March 2006; published 26 May 2006)

A table-top volumetric CT system has been implemented that is able to image a 5-cm-thick volume in one circular scan with no cone-beam artifacts. The prototype inverse-geometry CT (IGCT) scanner consists of a large-area, scanned x-ray source and a detector array that is smaller in the transverse direction. The IGCT geometry provides sufficient volumetric sampling because the source and detector have the same axial, or slice direction, extent. This paper describes the implementation of the table-top IGCT scanner, which is based on the NexRay Scanning-Beam Digital X-ray system (NexRay, Inc., Los Gatos, CA) and an investigation of the system performance. The alignment and flat-field calibration procedures are described, along with a summary of the reconstruction algorithm. The resolution and noise performance of the prototype IGCT system are studied through experiments and further supported by analytical predictions and simulations. To study the presence of cone-beam artifacts, a "Defrise" phantom was scanned on both the prototype IGCT scanner and a micro CT system with a ±5° cone angle for a 4.5-cm volume thickness. Images of inner ear specimens are presented and compared to those from clinical CT systems. Results showed that the prototype IGCT system has a 0.25-mm isotropic resolution and that noise comparable to that from a clinical scanner with equivalent spatial resolution is achievable. The measured MTF and noise values agreed reasonably well with theoretical predictions and computer simulations. The IGCT system was able to faithfully reconstruct the laminated pattern of the Defrise phantom while the micro CT system suffered severe cone-beam artifacts for the same object. The inner ear acquisition verified that the IGCT system can image a complex anatomical object, and the resulting images exhibited more high-resolution details than the clinical CT acquisition. Overall, the successful implementation of the prototype system supports the IGCT concept for single-rotation volumetric scanning free from cone-beam artifacts. © *2006 American Association of Physicists in Medicine*. [DOI: 10.1118/1.2192887]

Key words: volume CT, inverse-geometry CT, MTF, noise

I. INTRODUCTION

The ability to rapidly image an entire organ in one gantry rotation enables innovative and improved clinical applications such as dynamic studies. Acquiring a thick volume in one scan also reduces the motion artifacts and exam times compared to standard CT protocols.

For a conventional circular-scan CT geometry, the increased volume thickness is achieved by adding more rows to the detector and using a larger x-ray cone angle. However, there is a penalty for the improved coverage as exact reconstruction is not possible due to insufficient sampling of the volume. That is, a circular-scan cone-beam acquisition does not acquire sufficient volumetric data because of the diverging x-ray beam in the slice direction.[1] While approximate reconstruction algorithms are widely used,[2] the resulting artifacts increase with the volume thickness. The detected scattered radiation also increases with the detector size.

A possible solution for sufficient volumetric scanning without cone-beam artifacts is a line source which is scanned in the axial, or slice, direction opposite a large-area detector.[3] This geometry provides sufficient volumetric sampling, but is still prone to scatter artifacts. Also, the detector in this geometry must be extremely fast to isolate the measurements from the different source positions. Further, because the detector area is large, detector cost could be prohibitive.

We previously proposed an inverse-geometry CT (IGCT) system to acquire a volume on the order of several centimeters in a single fast rotation without cone-beam artifacts.[4] The system uses a large-area scanned source and a detector array which is smaller in the transverse, or in-plane, direc-

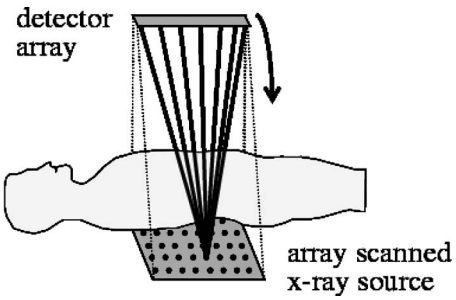

FIG. 1. Proposed IGCT geometry shown with the x-ray beam at one position in the source array.

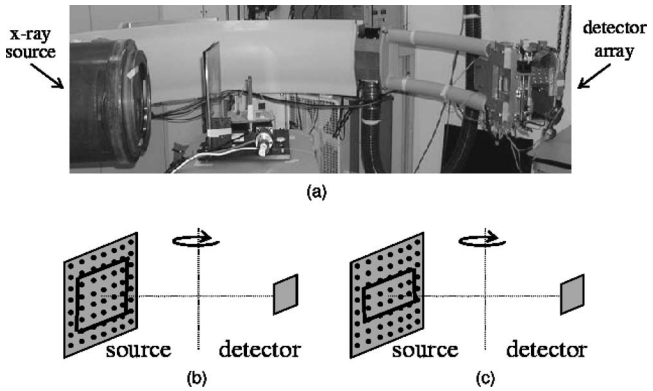

FIG. 2. (a) The prototype table-top IGCT scanner. The prototype system source is larger than the detector in both dimensions. A 16-cm × 16-cm subset of the source array (b) was used for all experiments, except for the noise experiments where 16 cm × 5 cm (c) of the source were used.

tion. The IGCT system avoids cone-beam artifacts by using a source and detector with the same axial extent as the volume being imaged. Additional scatter and cost benefits are possible because of the smaller detector area.

Previous work studied the feasibility of the IGCT system through simulations and explored a possible reconstruction algorithm.[4,5] This paper describes the implementation of a prototype table-top system. We first introduce the IGCT concept and describe the prototype system, including calibration considerations. We then investigate the resolution and noise performance of the prototype system through theoretical calculations, simulations, and experiments. The presence of cone-beam artifacts is tested and compared to a cone-beam system, and we present images of inner ear specimens acquired by the IGCT system and clinical multislice CT scanners.

II. METHODS AND MATERIALS

A. IGCT system

The proposed IGCT system consists of a CT gantry with a scanned-area source opposite a detector array, as illustrated in Fig. 1. The source and detector have the same axial, or slice-direction, extent, while the detector can be narrower in the transverse direction. During an acquisition an electron beam is electromagnetically steered across the transmission target of the source, dwelling behind each of an array of collimator holes that limits the resulting x-ray beam to those rays traveling toward the detector. For each source position the entire detector array is read, forming a two-dimensional (2D) image of a fraction of the field of view (FOV). The source scanning is rapid compared to the gantry rotation.

Scanning-beam x-ray systems have been implemented for both medical[6–8] and industrial[9,10] applications. An inverse-cone-beam CT geometry has been investigated for industrial applications.[11] The prototype table-top IGCT system was implemented using a NexRay Scanning-Beam Digital X-ray (SBDX) system (NexRay, Inc., Los Gatos, CA), which has a scanned source opposite a photon-counting detector array on a C-arm gantry.[6] The 23-cm × 23-cm transmission target is comprised of a thin-film layer of tungsten-rhenium on a beryllium substrate. The 5.4-cm × 5.4-cm direct-conversion detector is a tiled 4 × 4 array of detector hybrids, each hybrid consisting of a CdZnTe tile bump-bonded to a custom silicon IC containing the photon detection and counting circuitry for 144 1.14-mm × 1.14-mm detector elements.[12] The rapid source scanning requires very fast readout rates, since each detector has to be read for every source position (~1 MHz in our case). In addition, the use of photon counting requires very fast count rates (on the order of several million counts per second per channel). Photon-counting detectors are capable of achieving these speeds.[12] Photon counting detectors have the additional benefit of increased detective quantum efficiency compared to energy integrating detectors.[13]

The C-arm was positioned horizontally with a numerically controlled rotating stage placed between the source and detector, as shown in Fig. 2(a). Table I lists the specifications of the prototype system. In the IGCT geometry, the source and detector should have the same axial extent, thus providing sufficient volumetric sampling. With the SBDX system, whose source is larger than the detector in both dimensions, this requirement is met by restricting the axial FOV and using only the source positions within an axial extent that matches the detector size. In our initial implementation we restricted the axial FOV to 5 cm and used the central 16 cm, or 71 rows, of the source [Fig. 2(b)], except for the noise experiments where the central 5 cm of source rows were used [Fig. 2(c)]. Also, because the transverse extent of the

TABLE I. Prototype IGCT system specifications.

Source dimensions	23 cm × 23 cm
Source locations	100 × 100
Detector dimensions	5.4 cm × 5.4 cm
Detector elements	48 × 48
Source focal spot size (standard deviation)	0.183 mm
Detector aperture size	1.14 mm
Source power	25 kW
Dwell time per source location	1.04 μs
Move time between successive source locations	0.24 μs
Source-to-isocenter distance (SID)	45 cm
Source-to-detector distance (SDD)	150 cm
FOV (transverse × axial)	16 cm × 5 cm

TABLE II. Experimental setup (unless otherwise specified).

Source dimensions	16 cm × 16 cm
Source locations	71 × 71
FOV (transverse × axial)	10 cm × 5 cm
Source voltage	120 kVp
Source current	60 mA
Exposure time per source location per rotation angle	33.3 μs
Beam filtration	4.67 mm copper
Number of rotation angles	125
Total rotation	360°
Total exposure time	26 s

scanned objects was small, only 71 of the available 100 source columns were used, yielding a transverse FOV of 10 cm instead of the possible 16 cm.

Each acquisition consisted of 125 views equally spaced over 360°, as this number of views provides sufficient sampling.[4] The object was stationary during the acquisition of each view. A view consists of data acquired from all source positions and provides ray measurements spanning all radial locations and a range of azimuthal angles. For all experiments, the system operated at 120 kVp and 60 mA. Because the scanned objects had relatively low attenuation, and in order to prevent detector saturation, the source operated at approximately 7 kW instead of the maximum 25 kW. Also, to prevent detector saturation due to the small objects, the beam was further attenuated with 4.67 mm of copper, unless otherwise specified. This substantial copper filtration would not be needed for scanning a human-sized object. To model a system with higher count rate capability, and to ensure acceptable image quality, 32 frames were acquired and summed at each view angle, resulting in a 33 μs exposure time per source location per view angle. The total exposure time, not including the time required to move the stage, was 26 s. By utilizing only the source rows opposite the detector, as illustrated in Fig. 1, the exposure time would be reduced to 11 s. Note that because of collimation, each point in the object is exposed for a small fraction of the total time. The experimental setup is summarized in Table II.

B. Calibration

The critical geometric relationship in the prototype IGCT system is the location of the axis of rotation of the turntable with respect to the components on the C-arm. We assumed that the total misalignment could be characterized by four parameters defining the location and orientation of the axis of rotation.

A variety of methods have been proposed for geometric calibration of cone-beam CT systems.[14–19] The calibration of the IGCT system is based on elements adapted from a general cone-beam calibration method.[14] The method uses a phantom made of six 2.3-mm-diam stainless steel beads placed on a 4-cm-diam cardboard cylinder. The beads were spaced 2 cm apart in the slice direction. Eight views of the bead phantom were acquired over 360°, each comprised of the average of 160 frames. In addition to the axis of rotation, the three-dimensional locations of the beads were treated as unknowns. The forward problem, that is determining the projection of the beads given the source locations, bead locations, and axis of rotation, can be expressed analytically and is derived in the Appendix.

Each bead rotates in a circular trajectory, the center of which is the axis of rotation. Each IGCT view (rays connecting all sources to all detectors) provides some tomosynthetic information that can estimate the location of the beads at each stage position. The rays containing bead information were segmented from the calibration data through a combination of matched filtering and thresholding and used to estimate the bead trajectories and axis of rotation. A nonlinear least-squares algorithm was implemented to invert the forward expression derived in the Appendix and refine the estimates of the axis of rotation and bead locations. The calibration procedure was tested with simulated IGCT data of known alignment and realistic noise. With simulated data, the algorithm was able to estimate the geometry parameters to an accuracy on the order of tens of microns.

In addition to the alignment correction, a flat-field intensity calibration was performed to normalize the raw detector readings. The transmission through air was measured by averaging 3520 flat-field views. The averaged flat-field views provided individual correction factors for every ray connecting each source location to each detector independent of view angle.

C. Reconstruction algorithm

The IGCT data consist of in-plane rays, i.e., rays with a tilt angle of zero that connect each source row to the directly opposed detector row, and cross-plane rays that connect each source row to the remaining detector rows. This data set is geometrically similar to that of a multiring PET system. Therefore a modified three-dimensional (3D) PET algorithm is used for reconstruction.[20–22] During reconstruction, the data are first rebinned into 2D parallel-ray projections at multiple view and tilt angles, followed by a 3D filtered backprojection. Previous work studied the implementation of this algorithm for the IGCT system, including the artifact and resolution effects, and found the performance to be acceptable.[5] Therefore we only briefly summarize the algorithm here. The alignment parameters measured during calibration are incorporated into the rebinning algorithm and used to calculate the geometry of each ray in the IGCT system. Four geometric parameters describe each IGCT ray and determine the ideal 2D parallel-ray projection: the view angle, tilt angle, and the coordinates of the ray within the corresponding 2D parallel-ray projection, as illustrated in Fig. 3(a). Figure 3(b) illustrates the same parameters in the context of the IGCT geometry. Using these four parameters, each ray samples a point in a four-dimensional (4D) projection space. Rebinning the data into 2D parallel-ray projections is accomplished by gridding onto a Cartesian grid in the 4D projection space. Gridding, where data points within a defined bin-width are weighted based on a kernel shape

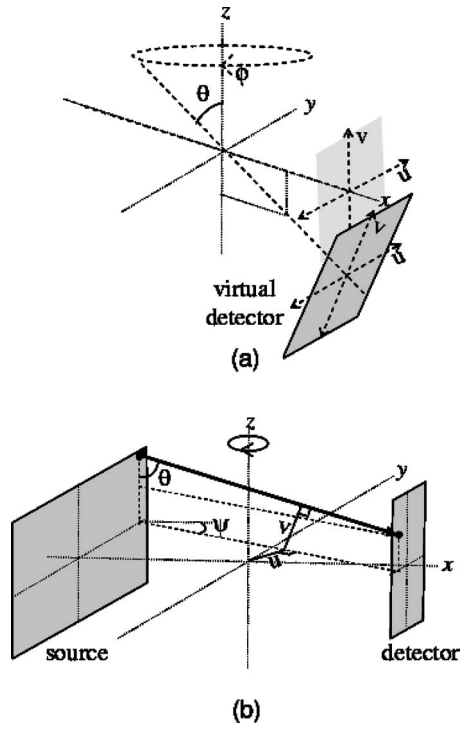

FIG. 3. (a) The 2D parallel-ray geometry to which the IGCT data are rebinned is illustrated using a virtual detector. ϕ is the projection view angle, θ is the tilt angle, and u and v are the coordinates within the projection. For comparison, two virtual detectors are shown, one with θ equal to $\pi/2$ and one with a smaller value of θ. (b) The four geometry parameters shown for a ray in the IGCT geometry where ψ is the azimuthal angle. The view angle, ϕ, is equal to the sum of the azimuthal angle and the gantry rotation angle.

and accumulated at the output grid points, is a discrete implementation of convolution followed by resampling.[23]

In our implementation, a separable 4D gridding kernel was defined as the product of four one-dimensional Hanning kernels. Each kernel was

$$h_g(x) = \frac{1}{w_g}\left(1 + \cos\left(\frac{2\pi x}{w_g}\right)\right)\mathrm{rect}\left(\frac{x}{w_g}\right), \tag{1}$$

where w_g is the kernel width, the kernel has been normalized to have an area of 1, and

$$\mathrm{rect}(x) = \begin{cases} 1 & |x| \le \frac{1}{2} \\ 0 & |x| > \frac{1}{2}. \end{cases}$$

The Fourier transform of the kernel is

$$H_g(k) = \mathrm{sinc}(w_g k) + \tfrac{1}{2}\,\mathrm{sinc}(w_g k - 1) + \tfrac{1}{2}\,\mathrm{sinc}(w_g k + 1). \tag{2}$$

The shape of the gridding kernel affects both the resolution and noise performance of the IGCT system. After data rebinning, the resulting projections are filtered with 2D filters designed to normalize the density of measurements in frequency space, followed by 3D backprojection. Unless otherwise stated, the reconstruction filter was multiplied by a Hanning window with a cutoff of 20 lp/cm. The parameters of the reconstruction algorithm are listed in Table III.

TABLE III. Reconstruction algorithm parameters (unless otherwise specified).

Number of rebinned views over 2π	1000 views
Maximum tilt angle of rebinned projections	0.02 rad
Tilt angle spacing	0.005 rad
2D parallel-ray projection sampling	0.125 mm × 0.125 mm
2D parallel-ray projection dimensions	4.4 cm × 10 cm
Gridding kernel width, radial directions	0.45 mm
Gridding kernel width, angular directions	0.0157 rad
Reconstruction filter window width	20 lp/cm

D. Resolution

1. Theoretical considerations

We began our study of the IGCT resolution by calculating the modulation transfer function (MTF) near the isocenter. The system resolution is determined by the source focal spot, detector aperture, geometric magnification, and the reconstruction algorithm. The effects of these factors on the resulting MTF can be described analytically.[24]

Figure 4 illustrates the relevant image space and frequency space coordinate systems.

We model the focal spot as a 2D Gaussian function with standard deviation S. To simplify our analysis, we consider only the central position in the IGCT source array and assume that all focal spots behave similarly. When a projection is acquired along the x direction, the impulse response at isocenter due to the finite spot size is

$$P_{\mathrm{source}}(x,y,z) = \exp\left(-\frac{1}{2}\left(\frac{\sqrt{y^2+z^2}\cdot \mathrm{SDD}}{S\cdot \mathrm{DID}}\right)^2\right), \tag{3}$$

where SDD is the source-to-detector distance and DID is the detector-to-isocenter distance. To further simplify our analysis, we calculate the MTF for a 2D parallel-ray projection with equivalent blur at isocenter. By assuming a parallel-ray geometry we can utilize the central slice theorem which

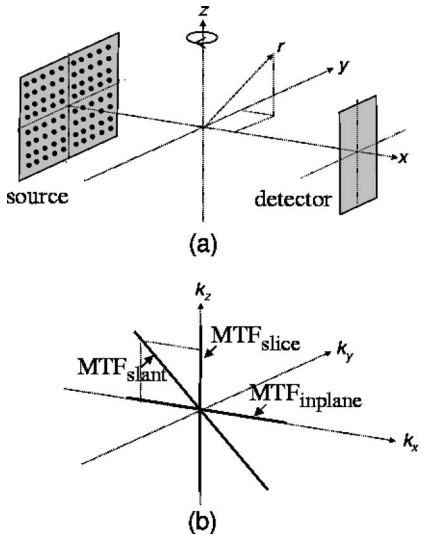

FIG. 4. The defined coordinate system in (a) image space and (b) frequency space labeled with the investigated MTF profiles.

states that a 2D parallel-ray projection samples the plane in frequency space that is perpendicular to the projection direction and that passes through the origin. Therefore, the MTF on the k_y-k_z plane in frequency space, and subsequently any plane containing the k_z axis, is the 2D Fourier transform of the blur function in Eq. (3), yielding the following 3D MTF:

$$\mathrm{MTF}_{\mathrm{source}}(k_x,k_y,k_z)=\exp\left(-2\left(\frac{\pi S\cdot \mathrm{DID}\cdot\sqrt{k_x^2+k_y^2+k_z^2}}{\mathrm{SDD}}\right)^2\right). \tag{4}$$

A similar effect is caused by the detector aperture, which we model as a square of length D. The resulting impulse response at isocenter for a projection in the x direction is

$$P_{\mathrm{detector}}(x,y,z)=\mathrm{rect}\left(\frac{y\cdot \mathrm{SDD}}{D\cdot \mathrm{SID}},\frac{z\cdot \mathrm{SDD}}{D\cdot \mathrm{SID}}\right), \tag{5}$$

where SID is the source-to-isocenter distance. The 3D MTF due to the detector blur is

$$\mathrm{MTF}_{\mathrm{detector}}(k_x,k_y,k_z)=\left(\mathrm{sinc}\left(\frac{\sqrt{k_x^2+k_y^2}\cdot D\cdot \mathrm{SID}}{\mathrm{SDD}},\frac{k_z\cdot D\cdot \mathrm{SID}}{\mathrm{SDD}}\right)\right). \tag{6}$$

In addition to these system effects, both the rebinning and filtering steps of the reconstruction algorithm contribute to the MTF. During rebinning, a convolution is performed in the 4D projection space which is defined by two distance and two angular components. In this analysis we consider only the effects of gridding the two distance parameters, that is the blurring within each 2D parallel-ray projection, as we are primarily focused on the resolution at isocenter where the angular blurring is negligible. The angular blurring would need to be considered when analyzing the resolution toward the edge of the FOV. By convolving with the gridding kernel within each 2D parallel-ray projection, we filter the corresponding plane in frequency space. To model the total effect in frequency space, planes from multiple view and tilt angles must be considered. Because the gridding kernel behaves similarly for all parallel-ray projections, and because the cross-plane rays acquired by the IGCT system have a relatively small tilt angle, we assume in this calculation only in-plane parallel-ray projections. We expect this simplification to be reasonably accurate when all the parallel-ray projections are considered. Based on the expression for the separable gridding kernel, $H_g(k)$, in Eqs. (1) and (2), each 2D parallel-ray projection is filtered with

$$H_{g2\mathrm{D}}(k_u,k_v)=H_g(k_u)\times H_g(k_v), \tag{7}$$

where k_u and k_v are the coordinates of the 2D Fourier transform of each projection. For the case of in-plane parallel ray projections, each of which samples a radial plane through frequency space (i.e., a plane that contains the k_z axis), the coordinates of each 2D projection are related to the 3D frequency space coordinates as

$$k_u=\sqrt{k_x^2+k_y^2}, \tag{8}$$

$$k_v=k_z, \tag{9}$$

and the total effect of the gridding algorithm on the 3D MTF is

$$\mathrm{MTF}_{\mathrm{grid}}(k_x,k_y,k_z)=H_g(\sqrt{k_x^2+k_y^2})\times H_g(k_z). \tag{10}$$

After rebinning, the 2D parallel-ray projections are filtered prior to backprojection. The 2D filters are designed to be the inverse density of measurements in frequency space and are apodized with a window function which affects the MTF. In our implementation, the window function is a 3D radial Hanning window of width W_f,

$$\mathrm{MTF}_{\mathrm{filt}}(k_x,k_y,k_z)=\frac{1}{2}\left(1+\cos\frac{2\pi\sqrt{k_x^2+k_y^2+k_z^2}}{W_f}\right). \tag{11}$$

The overall 3D MTF is the multiplication of the individual factors in Eqs. (4)–(11),

$$\mathrm{MTF}_{\mathrm{total}}=\mathrm{MTF}_{\mathrm{source}}\times\mathrm{MTF}_{\mathrm{detector}}\times\mathrm{MTF}_{\mathrm{grid}}\times\mathrm{MTF}_{\mathrm{filt}}. \tag{12}$$

The MTF is nearly isotropic, with the MTF in the in-plane direction the same as the MTF in the slice direction. Equation (12) is used as the theoretical reference.

2. Simulations

Noiseless IGCT data, for the system described in Table I, were simulated for a 76-μm-diam sphere at isocenter. The source focal spot and detector aperture were modeled using 9×9 discrete "source-lets" and 17×17 discrete "detector-lets." For each data point, line integrals for rays connecting each source-let to each detector-let were calculated assuming a monoenergetic beam and an attenuation coefficient of one. To model the IGCT components, the source-lets were averaged with a Gaussian weighting function of 0.183 mm standard deviation, and the detector-lets were averaged with a 1.14-mm rect function. An acquisition of 125 views was simulated and a volume of 2 cm $\times$ 0.1 cm $\times$ 2 cm and voxels of 0.0625 mm $\times$ 0.0625 mm $\times$ 0.0625 mm reconstructed with a Hanning windowed reconstruction filter with 80 lp/cm cutoff. In order to calculate the in-plane and slice MTF, the reconstructed volume was projected along the y

axis, and the 2D Fourier transform performed on the resulting projection, thus sampling the (k_x,k_z) plane in frequency space. The horizontal radial line through the 2D transform falls on the k_x axis and, when normalized, is the in-plane MTF, while the vertical radial line falls on the k_z axis and yields the slice MTF, as shown in Fig. 4.

3. Experiments

Two phantoms were designed for measuring the resolution of the prototype IGCT system. For measuring the in-plane MTF, a 76-μm-diam tungsten wire was manually aligned parallel and close to the axis of rotation in a plastic frame. Using a wire to measure the MTF in the slice direction, that is sampling the k_z axis in frequency space, is more challenging than in the in-plane direction. Theoretically, the wire could be positioned on a transverse plane (i.e., perpendicular to the axis of rotation). However, a wire aligned with the projection direction is difficult to image in practice because of the small cross section for photon penetration and significant attenuation across its length. The resulting x-ray projections would be highly nonlinear and could cause streak artifacts in the reconstructed image.[25]

We evaluated the MTF in the slice direction by using a wire slanted at 45° to the axis of rotation. Using this phantom, we can sample a radial line in frequency space at 45° to the k_z axis, labeled $\mathrm{MTF}_{\mathrm{slant}}$ in Fig. 4. This ray is neither the in-plane nor slice MTF, but does give some measure of the isotropy of the resolution.

For the vertical wire phantom, a volume of 0.25 cm $\times$0.25 cm$\times$1 cm centered at isocenter was reconstructed with voxels of 0.0625 mm$\times$0.0625 mm$\times$0.125 mm. The reconstructed volume was averaged along the slice direction followed by a 2D Fourier transform, thereby sampling the (k_x,k_y) plane in frequency space. Any radial line on this plane measures the in-plane MTF, and we chose to display the horizontal line corresponding to the k_x axis. An examination of the axial images found the wire alignment to be nearly vertical, therefore the slice averaging did not significantly degrade the resolution.

For the slanted wire phantom, a volume of 0.25 cm $\times$0.25 cm$\times$1 cm oriented perpendicularly to the wire was reconstructed with voxels of 0.0625 mm$\times$0.0625 mm $\times$0.125 mm. The volume was averaged in the direction of the wire and the 2D Fourier transform performed on the resulting projection, sampling the plane in frequency space that contains the k_y axis and is 45° to the k_z axis. The vertical radial line in this plane corresponds to $\mathrm{MTF}_{\mathrm{slant}}$ in Fig. 4. For both wire phantom reconstructions, the reconstruction filter was windowed with a Hanning window with 80 cycles/cm cutoff.

E. Noise

1. Theoretical considerations

The variance, σ^2, of a reconstructed CT voxel depends on the spatial resolution and the number of photons that passed through the object and were detected as expressed in

$$\sigma^2 = A \cdot \sum_{j=1}^{m} \frac{1}{N_j}, \tag{13}$$

where N_j is the mean detected photon fluence, photons per unit area, that has passed through the voxel in the jth projection, A is the integral of the square of the reconstruction filter, and m is the number of projections.[26] In this analysis we consider only noise due to photon-counting statistics and assume that the photon density, N, is constant across all projections.

In the specific case of volumetric reconstruction from in-plane 2D parallel-ray projections, that is 2D projections with rays perpendicular to the axis of rotation, A can be expressed as

$$A = \frac{\pi^2}{m^2} \int_{-\infty}^{\infty} \int_{-\infty}^{\infty} k_u^2 |W(\sqrt{k_u^2 + k_v^2})|^2 dk_u dk_v, \tag{14}$$

where W is the window function used to apodize the reconstruction filter, in our case a radial Hanning window of width W_f, and k_u and k_v are the coordinates of the Fourier transform of each 2D projection.

Equation (14) expresses the relationship between the detected photon density and the reconstructed noise for a 2D parallel-ray system. To more accurately represent the resolution of the IGCT system, Eq. (14) must be modified to incorporate the blur introduced during rebinning. As in the MTF analysis, we consider the effect of the gridding kernel in frequency space and model it as part of the reconstruction filter in Eq. (14). The effective reconstruction filter, $R(k_u,k_v)$, is

$$R(k_u,k_v) = |k_u| W(\sqrt{k_u^2 + k_v^2}) H_g(k_u) H_g(k_v), \tag{15}$$

where $H_g(k)$ is the gridding kernel defined in Eq. (2). The modified noise relationship is

$$\sigma^2 = \frac{\pi^2 \int_{-\infty}^{\infty} \int_{-\infty}^{\infty} |R(k_u,k_v)|^2 dk_u dk_v}{m \cdot N}. \tag{16}$$

Previous work found the photon utilization efficiency of the IGCT system to be equivalent to a 2D in-plane parallel-ray geometry.[5] That is, when simulated IGCT and parallel-ray systems of comparable resolution and FOV utilized the same number of photons, the resulting images had comparable noise. Based on these results, there is no penalty for using the IGCT system, and we can predict the noise in the IGCT system by calculating the noise for a comparable 2D parallel-ray system which uses the same total number of photons. Given the total number of photons and the rebinned parallel-ray sampling, the photon density can be computed and used in Eq. (16) to predict the noise for the IGCT system.

Since the IGCT system has no post-patient collimation or inter detector gaps, and since the x-ray beams can be collimated so that even the penumbra falls onto the detector, the system is expected to be very efficient in this regard.

2. Simulations

The assumption of monoenergetic x-rays was acceptable for the MTF simulations because the attenuation can be arbitrary and noise was not modeled. A model that considers the polyenergetic spectrum is required to predict the noise performance of the IGCT system. This was done using analytical CT simulations that employed a model of the detected x-ray spectrum generated using a Monte Carlo simulation of the source. This model, referred to as the "NexRay flux model," estimates the detected count rates as a function of tube power (kVp and mA) and object composition. In a previous unpublished study, Monte Carlo simulations of electron and photon transport (EGSnrc[27]) through the thin film transmission target were used to generate a 120 kVp polyenergetic x-ray spectrum with 1 keV energy bins. Beam quality of the spectrum was verified experimentally by measuring the attenuation properties of several materials, including copper, aluminum, and Lucite, with a solid state dosimeter (SolidDose 300). Due to its limited dynamic range, the NexRay detector cannot measure counts from an unattenuated entrance spectrum (i.e., an air scan) at typical power levels without saturating. Hence, to compute relevant entrance fluence rates, count rates were measured through 24 cm of Lucite and entrance flux was calculated numerically using photon cross sections for Lucite taken from the NIST XCOM database.[28] To predict detected count rates for different objects and filters of interest, the model entrance spectrum, having now been validated for beam quality and quantity (i.e., mean number of entrance photons/energy bin/detector element/ sample), was attenuated using appropriate XCOM coefficients. The expected count rate was then taken as the sum of the expected counts for all energy bins above 22 keV, which is the detector energy threshold cutoff.[12] Counts due to scatter were deemed negligible and thus not considered.[8]

Based on this model, IGCT data were simulated of Gaussian noise with mean and variance equal to the number of detected counts (the high number of detected counts allowed a Gaussian approximation to the Poisson photon statistics). The simulated IGCT geometry had the specifications listed in Table I, except that the source consisted of 21 source rows and 71 source columns. The central axial slice was reconstructed using the parameters in Table III. The IGCT simulations were repeated five times, and the mean measured noise level is reported.

3. Experiments

The investigation of the feasibility of the IGCT concept with respect to noise had two objectives. First we validated the theoretical and simulated noise predictions using a physical experiment with a water phantom. The water phantom experiment was intended to verify the noise prediction of Eq. (16), which assumes a known detected flux density. The NexRay flux model, which has been previously verified experimentally for a range of mA settings and attenuating objects, provides the estimated detected flux density. Once validated, the models were used to predict the noise performance of a potential clinical IGCT system compared to a conventional CT scanner.

An 11.15-cm-diam water sphere was scanned on the prototype IGCT system using a Lucite "bowtie" filter. The bowtie was designed to provide uniform detected intensity for the water sphere. The bowtie was mounted on the source and 1 mm of copper was used to further attenuate the beam. We measured the noise at the center of the reconstruction of the sphere, where the bowtie thickness was 1.27 cm.

The purpose of this experiment was to measure the noise in IGCT reconstructions. Therefore we aimed to reconstruct images containing only noise, without object-related artifacts that could result from, for example, misalignment between the sphere and the bowtie. Since 32 frames were acquired at each view angle, the acquired data were divided into two data sets each using the sum of 16 frames. The views in the first scan were normalized by the corresponding views in the second scan instead of by the flat-field calibration. This normalization removed the object from the projection and increased the noise by a factor of $\sqrt{2}$. Our reported noise measurements correct for this normalization factor but not for the noise penalty incurred by halving the number of frames. In order to better represent the noise performance of a clinical IGCT geometry, only data from the central 5 cm, or 21 rows, of the source were included in the reconstruction. The central axial slice of the water phantom was reconstructed with pixel spacing of $0.125\ \text{mm} \times 0.125\ \text{mm}$.

The mean number of detected photons per ray sample, P_d, was calculated for the measured data set and compared to that predicted by the NexRay model. Based on this number, the photon fluence was estimated at the entrance of the sphere using

$$F_{\text{IGCT}} = \frac{P_d \times S \times \text{SDD}^2}{\text{attn} \times \text{area}_{\text{det}} \times \text{DQE} \times \text{SOD}^2}, \tag{17}$$

where S is the number of ray samples that pass through the entrance of the object, attn is the estimated attenuation of the sphere, DQE is the estimated detective quantum efficiency of the NexRay detector, and SOD is the distance from the source to the sphere entrance. We estimated the mAs required for a conventional CT system to provide the same photon fluence at the object entrance by dividing F_{IGCT} by the flux density ($\text{photons}/\text{mm}^2\,\text{s}\,\text{mA}$) of a typical CT acquisition.[29]

A 35-cm polyethylene phantom was scanned on a single-slice scanner (CT/i, GE Healthcare, Milwaukee WI) with 0.625-mm in-plane resolution, 5-mm slice thickness, 120 kVp, 100 mA, and a 1-s scan time. A discussion on increasing the IGCT field of view is deferred to Sec. IV. Here we determine whether the IGCT system could provide the same noise as the single-slice acquisition for an object with attenuation equivalent to the 35-cm phantom and using reasonable source power. In order to make a fair comparison, the noise was predicted for an IGCT system with 0.625-mm in-plane resolution, 5-mm slice thickness, 95-cm source-to-detector distance, and a 1-s scan time. We assumed the IGCT

source array was comprised of 21×100 positions. Based on the timing parameters in Table I, and assuming one frame acquired at each IGCT view angle, the source array is scanned 372 times during the one second scan time. The calculation assumed the IGCT prototype components (i.e., same focal spot and detector aperture) and modified the resolution by matching the reconstruction filter cutoff to that of the noise power spectrum curve of the clinical reconstruction. In this calculation we used Eq. (16) to predict the detected photon density that would result in the measured noise value, followed by the NexRay flux model to calculate the mA corresponding to the detected number of photons.

F. Cone-beam artifacts

To verify that the IGCT system can acquire a thick volume without cone-beam artifacts, a "Defrise" phantom was constructed and scanned on the prototype system. The phantom was comprised of alternating Teflon™ and balsa wood disks, each of thickness 0.8 mm and diameter 2.5 cm, with a total height of 4.5 cm. The 4.5-cm × 5-cm central coronal slice of the phantom was reconstructed with voxels of 0.125 mm × 0.125 mm × 0.125 mm.

The Defrise phantom was also scanned on a cone-beam micro CT system (eXplore RS, GE Healthcare) with a ± 5° cone angle for the 4.5-cm volume thickness. Four hundred views were acquired at 80 kVp, 0.450 mA, 300 ms per view, and 90-μm isotropic resolution. The central coronal slice was reconstructed using a Feldkamp type algorithm[2] and voxels of 0.0514 mm × 0.0514 mm × 0.0514 mm.

G. Inner ear specimens

An inner ear specimen from a human cadaver was scanned on the IGCT system as well as a clinical CT scanner (Lightspeed 16, GE Healthcare) to test the performance of the IGCT system for more complex, anatomical objects. The clinical data were acquired in axial scan mode at 120 kVp and 400 mA with a 1-s scan time and 0.625-mm detector row spacing, and reconstructed using the standard kernel. For both data sets, the 4.5-cm volume was reconstructed with axial slices, with voxels of 0.125 mm × 0.125 mm × 0.125 mm for the IGCT acquisition and voxels of 0.1875 mm × 0.1875 mm × 0.625 mm for the conventional acquisition. A second specimen was scanned on an eight-slice clinical scanner (Lightspeed 8, GE Healthcare) and reconstructed using the bone-detail kernel. The eight-slice data were acquired at a helical pitch of one, 120 kVp, 200 mA, 1-s gantry rotation, and 0.625-mm in-plane resolution and slice thickness. The volume was reconstructed with axial slices with voxels of 0.195 mm × 0.195 mm × 0.625 mm. The IGCT data from the first specimen was reconstructed with a "standard" kernel (Hanning window with 20 lp/cm cutoff) and with a "high resolution" kernel (the inverse of a Hanning up to 14 lp/cm reaching zero at 27 lp/cm).

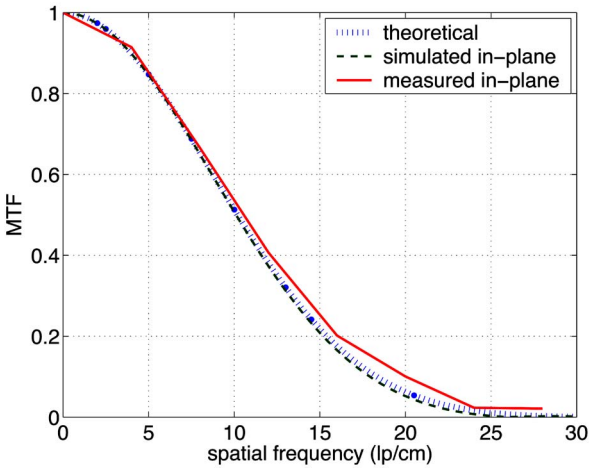

FIG. 5. A comparison of the theoretical, simulated, and measured in-plane MTF curves.

III. RESULTS

A. Resolution

Figure 5 compares the theoretically predicted, simulated, and measured in-plane MTF curves. A similar comparison is shown in Fig. 6 for the predicted slice MTF and measured MTF in the slanted direction. In both cases, the experimentally observed MTF is slightly better than that predicted analytically or by the simulations, with the 10% point being at 17 lp/cm in the prediction and at 20 lp/cm in the measurement. While the slight improvement in the IGCT MTF at high frequencies is still being investigated, there is reasonable agreement between the predicted and measured curves, and the resolution is isotropic.

B. Noise

The standard deviation of the water sphere noise image acquired by the prototype IGCT system was 80.4 HU. The NexRay flux model, for the parameters of the water sphere

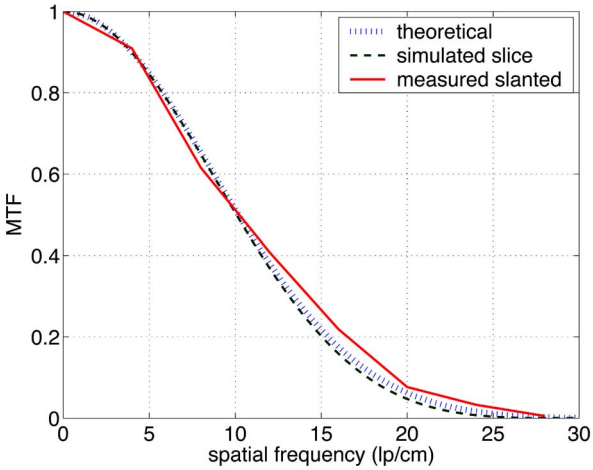

FIG. 6. A comparison of the theoretical and simulated slice MTF curves and the measured MTF which is slanted 45° from the k_z axis.

TABLE IV. Results of noise investigation.

	Theoretical noise (HU)	Simulated noise (HU)	Measured noise (HU)
1.4 counts per sample	74.8	73.3	
1.58 counts per sample	70.4	70.7	80.4

experimental setup (120 kVp, 60 mA, 1.04 μs per sample) predicted a detected intensity of 1.4 photons per sample per detector (in this experiment each ray is sampled 16 times for a total of 22.4 photons per ray) for the central slice of the sphere, in good agreement with a measured mean count rate of 1.58 photons per sample in the raw projection data (the measured count rate was obtained after correcting for the 10% double counts that are missed by the anti-coincidence circuitry[8]). Noisy IGCT data were simulated using both predicted and measured flux values. The average noise in the reconstructions, with 20 lp/cm filter cutoff and 1.4 counts per ray sample, was 73.3 HU. When taking into account the 1.4 detected photons per ray, 71 by 21 source spots, 48 by 48 detectors, 125 view angles, and 16 frames per view, the total number of photons in the IGCT acquisition was 9.62×10^9. If this same number of photons was distributed to a parallel-ray geometry but only into in-plane rays with projection sampling described in Table III, the resulting photon density per view would be 2190 photons/mm^2. Using Eq. (16), and assuming a reconstruction filter cutoff of 20 lp/cm, the predicted noise for the water sphere experiment is 74.8 HU. A summary of the measured, simulated, and theoretically predicted noise values is presented in Table IV. Understanding the slight discrepancy between the measured and predicted values, possibly due to instabilities in the source or detector, is an area of future work.

According to Eq. (17) and the analysis in Sec. II E 3, the IGCT acquisition had a photon fluence of 3.0×10^7 photons/mm^2 at the entrance of the water sphere, which is equivalent to an acquisition using a conventional CT scanner at a technique of 4.5 mAs. This calculation assumed 1.58 photons per detector per 1.04-μs sample, an estimated IGCT DQE of 0.78, and assumed that the entrance of the sphere surface in the conventional CT geometry is 50 cm from the source.

The measured noise may seem high for a relatively small object, however the images have 0.25-mm isotropic resolution and a very low effective mAs of 4.5. To determine whether the IGCT system could provide noise comparable to a conventional system, we calculate the mA needed by an IGCT system to achieve SNR equivalent to a clinical acquisition at the same spatial resolution. A noise standard deviation of 22.6 HU was measured for the 120-kVp, 100-mA, 1-s clinical acquisition of a 35-cm polyethylene phantom with 0.625-mm in-plane resolution, and 5-mm slice thickness. According to Eq. (16), a detected photon density of 124 photons/mm^2/view produces 22.6 HU noise standard deviation at this spatial resolution for a parallel-ray geometry (assuming 1000 views), which corresponds to 0.37 photons detected per ray in the IGCT system (assuming a 1-s IGCT scan, 21 by 100 sources spots, and the timing parameters listed in Table I). The NexRay flux model predicts that 150 mA is necessary to provide this detected flux for a 35-cm water object, 95-cm source-to-detector distance and 120-kVp acquisition. The IGCT system requires more source power to achieve the same SNR because each voxel is illuminated for a portion of the scan time, the fraction of time in which the source "sees" the voxel and the fraction of time that the beam is on. Nonetheless, the mA required for SNR comparable to the clinical acquisition is within the capabilities of the NexRay source. The results of the noise investigation suggest that the IGCT system can provide the same noise as a conventional system with comparable resolution, and further, that the parameters are physically achievable for reasonable protocols.

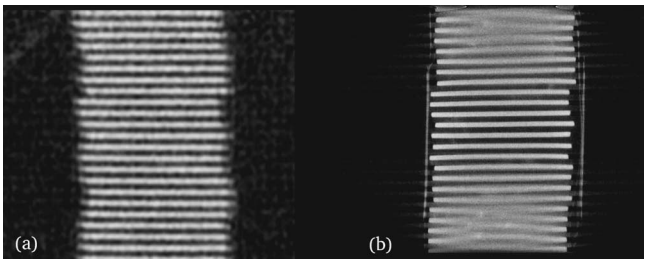

FIG. 7. A coronal image of the Defrise phantom acquired by (a) the IGCT system and (b) the GE eXplore RS micro CT system. Significant cone-beam artifacts can be seen in the micro CT reconstruction.

C. Cone-beam artifacts

Figure 7 compares coronal images of the Defrise phantom acquired by the IGCT and cone-beam micro CT systems. The micro CT scanner is designed for high-resolution and high dose acquisition, therefore the disks at the center of the volume are better depicted in the cone-beam acquisition. However, significant cone-beam artifacts are visible in the micro CT image toward the edge of the volume. In the IGCT acquisition, the disks are reconstructed uniformly throughout the volume, verifying that the IGCT system does not suffer from cone-beam effects.

D. Inner ear specimens

Selected images of the first inner ear specimen, acquired by both the IGCT and 16-slice systems, are shown in Fig. 8. The increased sharpness of the IGCT reconstruction is a result of both the higher in-plane resolution and the thinner slices compared to the clinical system. The clinical images, reconstructed with the "standard" reconstruction kernel, do not represent the highest resolution available on the scanner. Like the images from the clinical scanner, the IGCT data were also reconstructed with a relatively soft Hanning windowed reconstruction filter which also does not utilize the full system resolution. Although the ear images do not portray the best resolution of either system, we believe that Fig. 8 presents a valid comparison between the two systems. A

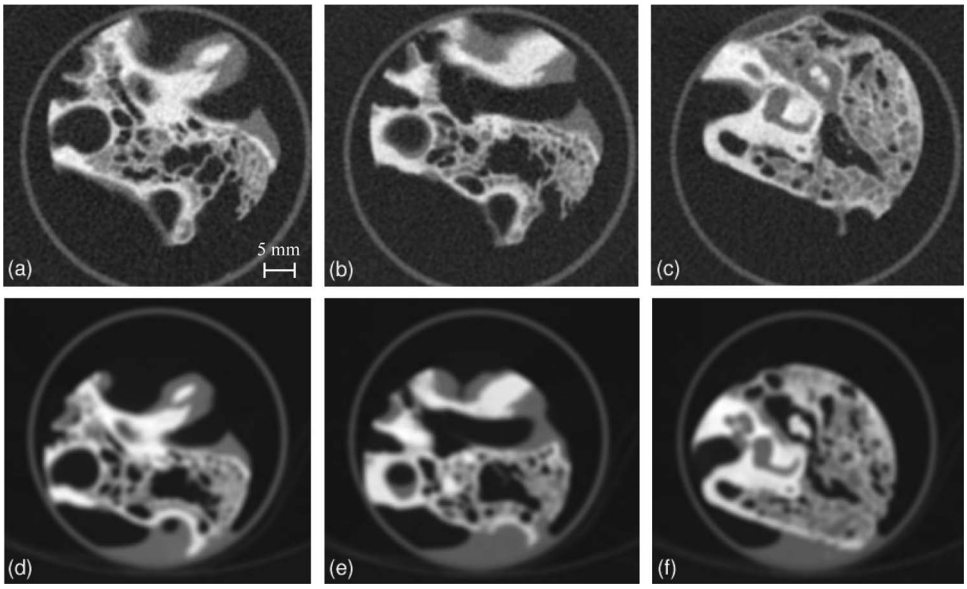

FIG. 8. Axial images of an inner ear specimen acquired by (a)–(c) the IGCT system and (d)–(f) a 16-slice scanner. Images were reconstructed with a standard kernel.

second ear specimen acquired on an eight-slice scanner and reconstructed with the "bone-detail" kernel is shown in Fig. 9, along with a similar slice from the IGCT acquisition of the first sample reconstructed with a high-frequency-enhancing kernel. The bone-detail kernel amplifies the noise in the IGCT reconstruction and the streak artifacts in the multislice reconstruction. Overall, the IGCT system successfully acquired and reconstructed the complex object with more high-resolution detail than the clinical scanner.

IV. DISCUSSION AND CONCLUSIONS

As the proposed IGCT system has a measurement geometry and hardware components that are new to CT, the successful implementation of the prototype system is a significant accomplishment in the development of the IGCT concept. However, the required further development to achieve a clinical IGCT system is substantial, and a discussion of how the results of the table-top investigation may apply to an IGCT system capable of scanning humans is in order, along with a discussion of the necessary future work.

The acquisition time of the initial experiments, on the order of tens of seconds, is unacceptably long for a human scanner. Presently, 32 frames are acquired per view angle to model a detector with higher count rate capability. Increasing the detector speed would reduce the scan time. Additionally, the FOV of the prototype system is greatly oversampled, and a significant reduction in scan time could be achieved by decreasing the number of source positions or interlacing the order of source row scanning. Previous work has studied an IGCT geometry with a 30-cm-wide in-plane FOV and 15-cm volume thickness using a 50-cm $\times$ 15-cm source array, and found that sufficient sampling and acceptable SNR are possible with a gantry rotation of less than 0.5 s.[4]

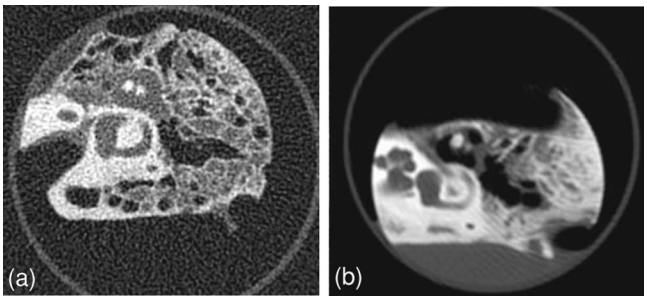

FIG. 9. Axial images of two inner ear specimens acquired by (a) the IGCT system and (b) an eight-slice scanner. Both images were reconstructed with a bone-detail kernel.

The prototype IGCT scanner has a relatively small in-plane FOV. Using a larger source array can increase the FOV, although the improved coverage may be at the expense of the scan time, sampling, or noise. When using a larger source array, a longer scan time is required to maintain the sampling within the FOV, although at present the FOV is greatly oversampled and some compromise is possible. The tube output remains constant as the source area increases, however the SNR may be reduced because each voxel in the object is illuminated for a smaller fraction of the scan time. A different approach for increasing the transverse FOV is to use multiple detector arrays spaced appropriately in angle. A multidetector IGCT system is currently being investigated which can acquire a 45-cm in-plane FOV using the 23-cm source array of the prototype system and three 5.4-cm-wide detector arrays.[30] By using the same source array, the scan time is unaffected, and if the three detectors can be illuminated simultaneously, the noise level will also be unaffected. Although a thorough analysis of the multidetector system is still in progress, we expect the noise performance for a 35-cm water phantom to be similar to that predicted in Sec. III B.

In the slice direction, the IGCT FOV can be increased by adding more source and detector rows. As the source and detector sizes increase, more oblique cross-plane rays can be collected. Because the in-plane rays span the full volume thickness and provide sufficient sampling, the oblique rays

can be used to improve the SNR. Therefore, the lack of cone-beam artifacts exhibited in Fig. 7 will be true for thicker volumes. Because more source positions are used, the scan time would need to be increased.

This paper investigated the resolution at isocenter, and the analysis in Sec. II D provides some insight as to the uniformity of the resolution across the FOV. As in a conventional system, the focal spot and aperture effects will vary with object location. This IGCT system uses a transmission target, and the apparent focal spot actually decreases away from the central ray. In addition, because the x-ray beam in the IGCT system is less divergent than a conventional system, the aperture variations across the FOV are smaller than in a conventional geometry. The angular gridding blur is an important effect which must be considered toward the edge of the FOV. We expect this effect to be relatively small and could be reduced by decreasing the gridding kernel width. Overall we expect the resolution to be fairly uniform across the FOV and experiments are planned to verify this prediction.

While an investigation of dose performance is outside the scope of the present paper, we expect the IGCT system to have higher dose efficiency than a conventional system. In a conventional CT geometry, a fraction of photons are lost due to interdetector gaps and post-patient collimation. In the IGCT system, the full detector area is utilized and there is no post-patient collimation. In addition, the IGCT x-ray beam is collimated so that almost all the photons strike the detector including the penumbra. Therefore, the detective geometric efficiency of the IGCT system is essentially one, which reduces the dose for a specified SNR compared to a conventional system. The increased DQE of photon-counting detectors compared to energy-integrating detectors[13] further reduces the dose, as does the increased scatter rejection due to the smaller detector area. A thorough investigation of the dose performance is required to quantitate these effects.

Considerable work remains to extend the IGCT concept to clinical applications. The prototype system must be further characterized including the low-contrast detectability, scatter, and dose performance, and an investigation must be performed of the technical challenges of operating the components on a high speed gantry. A geometry capable of imaging a large FOV must be optimized with respect to the source and detector sizes, sampling, resolution, noise, and scan times. Future work must also focus on increasing the dynamic range of the system, which includes improving the detector speed and designing spatially dependent attenuators. Depending on the optimal focal spot size, it may be possible to increase the source power, in which case this aspect would also have to be designed. Thus, implementing a prototype gantry-based IGCT system requires substantial engineering work, followed by an extensive performance evaluation.

The implementation of the prototype table-top IGCT system is the first step in supporting the feasibility of a scanner that can sufficiently sample a thick volume in one fast gantry rotation. The investigations presented in this paper, based on theoretical considerations, simulations, and experiments, demonstrate that the prototype system can successfully image a complex anatomical object with 0.25-mm isotropic resolution, noise comparable to a conventional system, and no cone-beam artifacts.

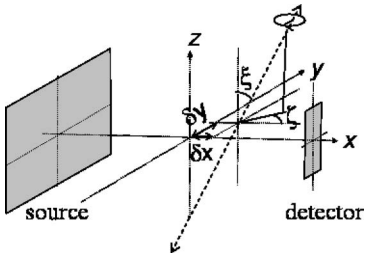

FIG. 10. The IGCT geometry with a misaligned axis of rotation depicted as a dashed line. The parameters δx, δy, ζ, and ξ define the location and orientation of the axis. The misalignment is exaggerated in this drawing.

ACKNOWLEDGMENTS

This work is supported by GE Healthcare. N.J.P. owns stock in GE. The authors would like to thank Jeff Dormo of Stanford University for help with the noise investigation, and Brian Wilfley of NexRay Inc., for assistance with the flux model.

APPENDIX: GEOMETRIC CALIBRATION

In this section we analyze the misaligned IGCT geometry and derive the forward expression for determining the bead projections given the source locations, bead locations, and the location of the axis of rotation. Figure 10 illustrates the misaligned IGCT geometry. We assume that the source and detector arrays are parallel and aligned at their centers and that the only source of misalignment is the location and orientation of the axis of rotation, shown as the dashed line in Fig. 10. Two distance parameters, δx and δy, define the point where the axis crosses the central plane of the source and detector. The orientation of the axis of rotation is parametrized by two angles, a rotation of ξ about a line parallel to the y axis, followed by a rotation of ζ about a line parallel to the z axis.

We define the source coordinates (s_x, s_y, s_z) and the bead center (b_x, b_y, b_z). We wish to calculate the point, (d_x, d_y, d_z), which is the projection of the bead center onto the detector for a given view angle ϕ.

To simplify our analysis we assume that the bead object is being rotated instead of the gantry. The coordinates of the bead center after a rotation of ϕ about the misaligned axis is

$$\begin{bmatrix} \hat{b}_x \\ \hat{b}_y \\ \hat{b}_z \end{bmatrix} = \mathbf{M_z}(-\zeta)\mathbf{M_y}(-\xi)\mathbf{M_z}(\phi)\mathbf{M}_y(\xi)\mathbf{M}_z(\zeta)\begin{bmatrix} b_x - \delta x \\ b_y - \delta y \\ b_z \end{bmatrix}, \tag{A1}$$

where $\mathbf{M_y}$ is the matrix defining a left-handed rotation about the y axis and $\mathbf{M_z}$ is the matrix defining a left-handed rotation about the z axis,

$$\mathbf{M_y}(\theta)=\begin{bmatrix}\cos(\theta) & 0 & -\sin(\theta)\\ 0 & 1 & 0\\ \sin(\theta) & 0 & \cos(\theta)\end{bmatrix}, \tag{A2}$$

$$\mathbf{M_z}(\theta)=\begin{bmatrix}\cos(\theta) & \sin(\theta) & 0\\ -\sin(\theta) & \cos(\theta) & 0\\ 0 & 0 & 1\end{bmatrix}. \tag{A3}$$

The source location and bead center define a line, and the projection of the bead center onto the detector is also on this line. Therefore

$$\begin{bmatrix}d_x\\ d_y\\ d_z\end{bmatrix}=\begin{bmatrix}\hat{b}_x-s_x+\delta_x\\ \hat{b}_y-s_y+\delta_y\\ \hat{b}_z\end{bmatrix}t+\begin{bmatrix}s_x\\ s_y\\ s_z\end{bmatrix}. \tag{A4}$$

Because $d_x=\mathrm{DID}$ and $s_x=-\mathrm{SID}$, we can solve for t,

$$t=\frac{\mathrm{DID}+\mathrm{SID}}{\hat{b}_x+\mathrm{SID}+\delta x}. \tag{A5}$$

Using Eqs. (A1)–(A5), we can solve the forward problem of determining the bead center projections given the source locations, bead locations, and axis of rotation. The calibration procedure described in Sec. II B inverts this expression using a nonlinear least-squares algorithm to find the axis of rotation and bead centers given the source and detector coordinates.

[a]Also at Department of Electrical Engineering. Electronic mail: taly.gilat-schmidt@marquette.edu
[b]Also at Department of Bioengineering.

[1]B. D. Smith, "Cone-beam tomography: Recent advances and a tutorial review," Opt. Eng. (Bellingham) **29**, 524–534 (l990).
[2]L. A. Feldkamp, L. C. Davis, and J. W. Kress, "Practical cone-beam algorithm," J. Opt. Soc. Am. A **1**, 612–619 (1984).
[3]E. Hell, P. Schard, and G. Schwierz, "X-ray computed tomography apparatus." U. S. Patent 5,841,831, 1998.
[4]T. G. Schmidt, R. Fahrig, E. G. Solomon, and N. J. Pelc, "An inverse-geometry volumetric CT system with a large-area scanned source: A feasibility study," Med. Phys. **31**(9), 2623–2627 (2004).
[5]T. G. Schmidt, R. Fahrig, and N. J. Pelc, "A three-dimensional reconstruction algorithm for an inverse-geometry volumetric CT system," Med. Phys. **32**(11), 3234–3245 (2005).
[6]E. G. Solomon, B. P. Wilfley, M. S. Van Lysel, A. W. Joseph, and J. A. Heanue, "Scanning-beam digital x-ray (SBDX) system for cardiac angiography," in *Medical Imaging 1999: Physics of Medical Imaging* [Proc. SPIE **3659**, 246–257 (1999)].
[7]M. A. Speidel, B. P. Wilfley, J. A. Heanue, T. D. Betttts, and M. S. V. Lysel, "Comparison of vessel contrast measured with a scanning-beam digital x-ray system and an image intensifier/television system," Med. Phys. **28**(2), 232–240 (2001).
[8]M. A. Speidel, "Performance characteristics of the scanning-beam digital x-ray SBDX cardiac imaging system," Ph.D. thesis, University of Wisconsin, UMI, 2003.
[9]R. D. Albert, "X-ray scanning method and apparatus," U. S. Patent 3,949,229, 1976.
[10]R. D. Albert and T. M. Albert, "NDT solution: Aerospace applications of x-ray system using reverse geometry," Mater. Eval. **51**, 1350–1352 (1993).
[11]M. D. Silver, R. Albert, and D. Reyna, "Reverse geometry volume computed tomography," in *1994 ASNT Spring Conference and Third Annual Research Symposium Professional Program*, pp. 79–81.
[12]J. Heanue, D. Pearson, and R. Melen, "CdZnTe detector array for a scanning-beam digital x-ray system," in Ref. 6, pp. 718–725.
[13]M. J. Tapiovaara and R. F. Wagner, "SNR and DQE analysis of broad spectrum x-ray imaging," Phys. Med. Biol. **30**(6), 519–529 (1985).
[14]G. T. Gullberg, B. M. W. Tsui, C. R. Crawford, J. G. Ballard, and J. T. Hagius, "Estimation of geometrical parameters and collimator evaluation for cone beam tomography," Med. Phys. **17**(3), 264–272 (1990).
[15]A. Rouge, C. Picard, C. Ponchut, and Y. Trousset, "Geometrical calibration of x-ray imaging chains for three-dimensional reconstruction," Comput. Med. Imaging Graph. **17**, 295–300 (1993).
[16]A. V. Bronnikov, "Virtual alignment of x-ray cone-beam tomography system using two calibration aperture measurements," Opt. Eng. (Bellingham) **38**, 381–386 (1999).
[17]F. Noo, R. Clackdoyle, C. Mennessier, T. A. White, and T. J. Roney, "Analytic method based on identification of ellipse parameters for scanner calibration in cone-beam tomography," Phys. Med. Biol. **45**, 3489–3508 (2000).
[18]L. von Smekal, M. Kachelriess, E. Stepina, and W. A. Kalender, "Geometric misalignment and calibration in cone-beam tomography," Med. Phys. **31**(12), 3242–3266 (2004).
[19]Y. Cho, D. J. Moseley, J. H. Siewerdsen, and D. A. Jaffray, "Accurate technique for complete geometric calibration of cone-beam computed tomography systems," Med. Phys. **32**(4), 968–983 (2005).
[20]M. Defrise, D. W. Townsend, and R. Clack, "Three-dimensional image reconstruction from complete projections," Phys. Med. Biol. **34**(5), 573–587 (1989).
[21]J. G. Colsher, "Fully three-dimensional positron emission tomography," Phys. Med. Biol. **25**(1), 103–115 (1979).
[22]N. J. Pelc, "A generalized filtered backprojection algorithm for three dimensional reconstruction," Ph.D. thesis, Harvard University, 1979.
[23]J. I. Jackson, C. H. Meyer, D. G. Nishimura, and A. Macovski, "Selection of a convolution function for Fourier inversion using gridding," IEEE Trans. Med. Imaging **10**, 473–478 (1991).
[24]C. C. Shaw, X. Liu, M. Lemacks, J. X. Rong, and G. J. Whitman, "Optimization of MTF and DQE in magnification radiography - A theoretical analysis," in *Medical Imaging 2000: Physics of Medical Imaging* [Proc. SPIE **3977**, 466–475 (2000)].
[25]G. H. Glover and N. J. Pelc, "Nonlinear partial volume artifacts in x-ray computed tomography," Med. Phys. **7**(5), 238–248 (1980).
[26]D. A. Chesler, S. J. Riederer, and N. J. Pelc, "Noise due to photon counting statistics in computed x-ray tomography," J. Comput. Assist. Tomogr. **1**, 64–74 (1977).
[27]I. Kawrakow and D. W. O. Rogers, "The EGSnrc code system: Monte Carlo simulation of electron and photon transport," NRCC Report No. PIRS-701, National Research Council of Canada, Ottawa, 2000.
[28]"NIST XCOM: Photon Cross Sections Database," National Institute of Standards and Technology, Gaithersburg, http://physics.nist.gov/PhysRefData/Xcom/Text/XCOM.html.
[29]J. A. Seibert, "X-ray imaging physics for nuclear medicine technologists. 1. Basic principles of x-ray production," J. Nucl. Med. Technol. **32**(3), 139–147 (2004).
[30]S. Mazin, T. G. Schmidt, E. G. Solomon, R. Fahrig, and N. J. Pelc, "Geometry analysis of an inverse-geometry volumetric CT system with multiple detector arrays," in *Medical Imaging 2004: Physics of Medical Imaging* [Proc. SPIE **5368**, 320–329 (2004)].